Journal of Alloys and Compounds 509 (2011) 4394–4398

Contents lists available at ScienceDirect

Journal of Alloys and Compounds

journal homepage: www.elsevier.com/locate/jallcom

Influence of chromium substitution on structural and magnetic properties of $BaFe_{12}O_{19}$ powder prepared by sol–gel auto combustion method

Vinod N. Dhage, M.L. Mane, M.K. Babrekar, C.M. Kale, K.M. Jadhav*

Department of Physics, Dr. Babasaheb Ambedkar Marathwada University, Aurangabad 431004, M.S., India

ARTICLE INFO

Article history:
Received 15 July 2010
Received in revised form
21 December 2010
Accepted 8 January 2011
Available online 14 January 2011

PACS:
75.50.Gg
74.25.Ld
43.35.Cg

Keywords:
Barium hexaferrite
Sol–gel
Nanocrystalline
Magnetization

ABSTRACT

The nanocrystalline Cr^{3+} substituted barium hexaferrite having generic formula $BaFe_{12-x}Cr_xO_{19}$ (where $x = 0.00, 0.25, 0.50, 0.75$, and 1.00) samples were synthesized by sol–gel auto-combustion technique. The precursors were prepared by using stoichiometric amounts of Ba^{2+}, Fe^{3+} and Cr^{3+} nitrate solutions with citric acid as a chelating agent. The metal nitrate to citric acid ratio was taken as 1:2 while pH of the solution was kept at 8. The thermal decomposition of nitrate–citrate gels of as-prepared powder was investigated by TG/DTA. The as-prepared powder of $BaFe_{12-x}Cr_xO_{19}$ was sintered at 900 °C for 8 h. The sintered powder was characterized by XRD, EDAX, SEM and VSM technique. The pure barium hexaferrite shows only single phase hexagonal structure, while for the samples at $x = 0.25$, 0.50, 0.75 and 1.00 shows α-Fe_2O_3 peaks with M-phase of barium hexaferrite. The lattice parameters (a and c) decreases with increase in chromium content x. The particle size obtained from XRD data is in the range of 30–40 nm which confirms the nanocrystalline nature of the samples. The magnetic properties were investigated by means of vibrating sample magnetometer (VSM) technique. The saturation magnetization (M_s), remanence magnetization (M_r), coercivity (H_c) and magneton number (n_B) decreases with increase in chromium content x.

1. Introduction

Barium hexaferrite ($BaFe_{12}O_{19}$) is a hexagonal M-type magnetoplumbite ferrimagnetic ceramic material with an easy magnetization along the c-axis. It is commonly used as permanent magnets particulate media for magnetic recording as well as in microwave devices [1–3]. Hexagonal ferrites are divided into six different types M($AFe_{12}O_{19}$), W($AMe_2Fe_{16}O_{27}$), X($A_2Me_2Fe_{28}O_{46}$), Y($A_2Me_2Fe_{12}O_{22}$), Z($A_3Me_2Fe_{24}O_{41}$), U($A_4Me_2Fe_{36}O_{60}$) where A = Ba, Sr, Pb, etc. and Me = is a divalent transition metal [4]. Among these types barium hexaferrite is widely used due to its low production cost combined with excellent magnetic properties. It has a high Curie temperature, a high coercive force and magneto crystalline anisotropy along the c-axis and is chemically stable and corrosion resistant. It is used to prepare sensors and microwave absorbing materials [5–9]. Moreover, due to their high anisotropy field hexaferrites can be used at much higher frequencies than spinel ferrites and garnets [10], for this reason they are interesting above 30 GHz. On account of their superior chemical stability, mechanical hardness, excellent corrosion resistance and low level of media noise, they are suitable for rigid disc media without protective and lubricant layers. Due to large magneto crystalline anisotropy and strong dependence of the orientation of easy axis on the microstructure, they have potential for application in both perpendicular and longitudinal magnetic recording media [11,12].

Various synthesis methods have been developed to prepare fine barium hexaferrite powders with the desired particle size and magnetic characteristics. These methods includes co-precipitation method [13,14], glass crystallization [15], hydrothermal [16], sol–gel auto combustion [17,18], microemulsion [19], citrate precursor [20], aerosol process [21] and spray pyrolysis technique [22,23]. Although these methods leads to formation of nanosize particles and good magnetic properties, many of these methods has some drawbacks or limitations. Among these methods, the sol–gel auto combustion method ensures the proper distribution of various metal ions resulting into stoichiometric and smaller particle size product compared to above other methods. Huang et al. [24] first reported the work on synthesis of fine $BaFe_{12}O_{19}$ powders using citric acid–nitrate sol–gel auto combustion followed by a secondary heat treatment. Many investigators [25,26] have synthesized $BaFe_{12}O_{19}$ nanocrystalline powder by probing the influences from metal nitrate to citric acid ratios as well as the pH values [27,28].

In the present study, the stoichiometric proportion of metal nitrate to citric acid has been used to prepare barium hexaferrite samples. The pure nanocrystalline barium hexaferrite

* Corresponding author. Tel.: +91 02402488988; fax: +91 02402403113.
E-mail address: drkmjadhav@yahoo.com (K.M. Jadhav).

0925-8388/$ – see front matter © 2011 Elsevier B.V. All rights reserved.
doi:10.1016/j.jallcom.2011.01.040

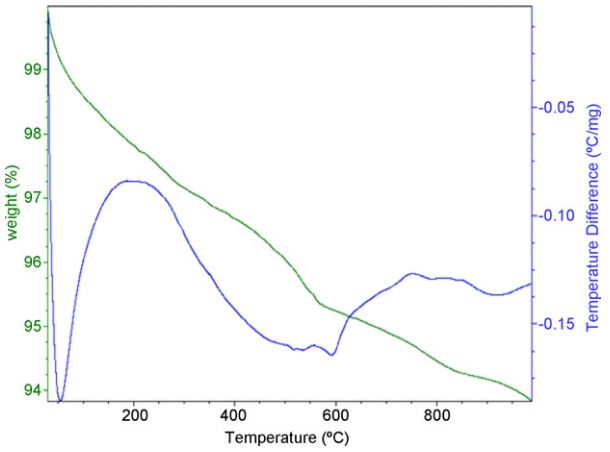

Fig. 1. Thermogravimatric analysis and differential thermal analysis of $BaFe_{12}O_{19}$ sample.

has been studied by many workers. However, the Cr^{3+} substituted nanocrystalline barium hexaferrite has not been studied in detail. In order to understand the role of chromium in barium hexaferrite matrix an investigated was done in the present work.

2. Experimental

Nanocrystalline chromium substituted barium hexaferrite samples were prepared by sol–gel auto combustion technique. AR grade barium nitrate $Ba(NO_3)_2$, ferric nitrate $Fe(NO_3)_3{\cdot}9H_2O$, chromium nitrate $Cr(NO_3)_3{\cdot}9H_2O$ were dissolved in minimum amount of deionised water. Citric acid ($C_6H_8O_7$) was then added into the prepared aqueous solution to chelate Ba^{2+} and Fe^{3+} ions in the solution. The metal nitrate to citric acid ratio was kept as 1:2 and then the pH of the mixed solution was kept at 8 by adding ammonia solution. The mixed solution was evaporated to dryness by heating at 100 °C on a hot plate with continuous stirring and finally formed a very viscous brown gel. This viscous brown gel was ignited by increasing the temperature up to 150 °C and the loose powder of the samples was obtained. Finally, the as burnt powder was sintered at 900 °C for 8 h to obtain chromium substituted barium hexaferrite nanoparticles.

The thermal decomposition behaviour of the as prepared powder was examined by simultaneous TG/DTA analysis. The phase identification of the prepared samples was performed with the help of Philips X-ray diffractometer (Model PW-3710) using Cu Kα radiation (λ = 1.5405 Å). The stoichiometric proportion of the constituent ions was examined through EDAX technique. The surface morphology of the prepared samples was studied by using scanning electron microscopy (Model JEOL-JSM 63604) technique. The magnetic parameters such as saturation magnetization (M_s), remenant magnetization (M_r), and coercivity (H_c) were obtained at room temperature by vibrational sample magnetometer (VSM) technique with maximum applied field of 9 kOe.

3. Results and discussion

3.1. Thermal analysis

The TG-DTA plot for the as synthesized powder is shown in Fig. 1. An endothermic reaction with weight loss is observed at around 100 °C corresponds to the evaporation of water in the samples. The exothermic peak at the onset temperature of 200 °C in the DTA curve corresponds to the crystallization of the M-phase of the barium hexaferrite nanoparticles. From TGA curve a weight loss of 25% was observed over the temperature region 50–500 °C. From 550 °C onwards there is a small weight loss ≈5% upto 575 °C. Two distinct weight loss steps around 50–500 and 750–950 °C were observed, which were attributed to the decomposition of hydroxides and barium nitrate, respectively. Above 950 °C no further indistinguishable weight loss was detected indicating that all organic constituents were eliminated.

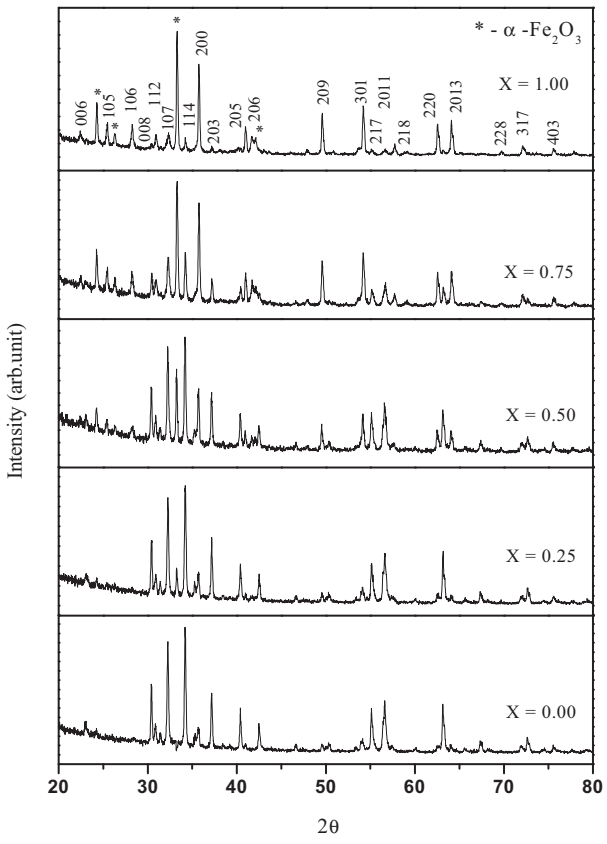

Fig. 2. X-ray diffraction patterns of $BaFe_{12-x}Cr_xO_{19}$ samples.

3.2. Structural analysis

Fig. 2 shows the X-ray diffraction patterns of the $BaFe_{12-x}Cr_xO_{19}$ (where x = 0.00, 0.25, 0. 50, 0.75 and 1.00) M-type hexaferrite samples. The $BaFe_{12}O_{19}$ (x = 0.00) sample shows single phase hexagonal structure while Cr^{3+} substituted $BaFe_{12}O_{19}$ samples shows α-Fe_2O_3 as a secondary phase. The presence of α-Fe_2O_3 peaks in barium hexaferrite matrix is also reported in the literature [29]. The X-ray diffraction pattern for pure $BaFe_{12}O_{19}$ is in good agreement with JCPDS data (file no. 84-0757). Using the JCPDS data the peaks of the XRD pattern were indices for hexagonal structure. However, the change in the relative intensities of the patterns may be related to occupation of the crystallographic sites of the crystal lattice. Lattice parameters a and c for all the samples were calculated by using the formula [30]:

$$\frac{1}{d^2} = \frac{4}{3}\left(\frac{h^2 + hk + k^2}{a^2}\right) + \frac{l^2}{c^2} \quad (1)$$

where 'd' is the interplaner spacing and hkl are the Miller indices. The values of lattice parameters are given in Table 1. It is evident from the values of lattice parameters a and c that both lattice parameters goes on decreasing with increase in the Cr content

Table 1
Lattice constant 'a' and 'c', c/a ratio and cell volume (V) of $BaFe_{12-x}Cr_xO_{19}$ samples.

Comp. 'x'	Lattice constant (Å)		c/a	V (Å)^3
	a	c		
0.00	5.8790	23.1410	3.9362	692.655
0.25	5.8785	23.1320	3.9350	692.268
0.50	5.8768	23.1290	3.9355	691.759
0.75	5.8759	23.1157	3.9339	691.168
1.00	5.8747	23.1056	3.9330	690.584

Table 2
X-ray density (d_x), bulk density (d_m), porosity (P), particle size (t) and grain size (G) of $BaFe_{12-x}Cr_xO_{19}$ samples.

Comp. 'x'	d_x (g/cm^3)	d_m (g/cm^3)	P (%)	t (nm)	G (nm)
0.00	5.3284	3.5342	33.6709	37.98	60
0.25	5.3267	3.4943	34.3989	34.53	55
0.50	5.3260	3.4665	34.9119	32.44	51
0.75	5.3259	3.4377	35.4522	31.65	46
1.00	5.3258	3.4259	35.6717	30.24	41

x. The decrease in the lattice parameters with the addition of chromium is due to replacement of higher ionic radii element Fe^{3+} (0.67 Å) by smaller ionic radii element Cr^{3+} (0.63 Å). Similar results were observed by substitution of Fe^{3+} (0.67 Å) by Mn^{3+} (0.645 Å) ions in barium hexaferrite [31]. This result shows that the crystal structures of barium hexaferrites were contracted after being doped with Cr^{3+} ions. Particle size (t) is obtained with the help of FWHM of most intense peak of the XRD pattern by using Scherrer formula [32]:

$$t = \frac{0.9\lambda}{\beta \cos\theta} \quad (2)$$

where β is the FWHM and λ is the wavelength of the target material.

The particle size obtained from the XRD data is in the range of 30–40 nm. The values of particle size is listed in Table 2. The bulk density of all the samples was measured by using well known Archimedes method and the values are presented in Table 2. The X-ray density (d_x) was calculated according to the relation [30]

$$d_x = \frac{2M}{N_a V_{cell}} \quad (3)$$

where numeric factor denotes the number of formula units in a unit cell, M is the molar mass, N_a is the Avogadro's number and V_{cell} is the unit cell volume computed from the values of lattice constants a and c as [30]:

$$V_{cell} = \frac{\sqrt{3}}{2} a^2 c \quad (4)$$

The values of unit cell volume and X-ray density are given in Tables 1 and 2, respectively. The unit cell volume and X-ray density both decreases with increase in Cr^{3+} content x. This behaviour of X-ray density is attributed to the fact that cell volume decreases more than the negligible rise in the molar masses of the doped metal cations. The values of measured density (d_m) are smaller than that of the X-ray density which is due to the presence of unavoidable pores during the heating process. The porosity (P) was calculated by using the following formula [30]:

$$P(\%) = \left(1 - \frac{d_m}{d_x}\right) \times 100 \quad (5)$$

The porosity of the samples increases with increase in Cr^{3+} substitution x. The increase in the porosity indicates that the doped elements may have retarded the process of densification of the hexaferrite matrix. The energy dispersive X-ray analysis plots for typical samples are shown in Fig. 3. The EDAX plots gives the evidence of Ba^{2+}, Fe^{3+}, Cr^{3+} ions with proper ratio confirming the desired stoichiometric composition. The α-Fe_2O_3 peak was also seen in the energy dispersive X-ray analysis plots [27].

3.3. Microstructural analysis

The surface morphology and microstructure of $BaFe_{12-x}Cr_xO_{19}$ of typical samples x = 0.00, 0.50, 1.00 nanomaterials were observed by scanning electron microscopy (SEM) as depicted in Fig. 4. The surface of synthesized samples was appears to be a mixture of individual nanoparticles of well crystalline nature and aggregates

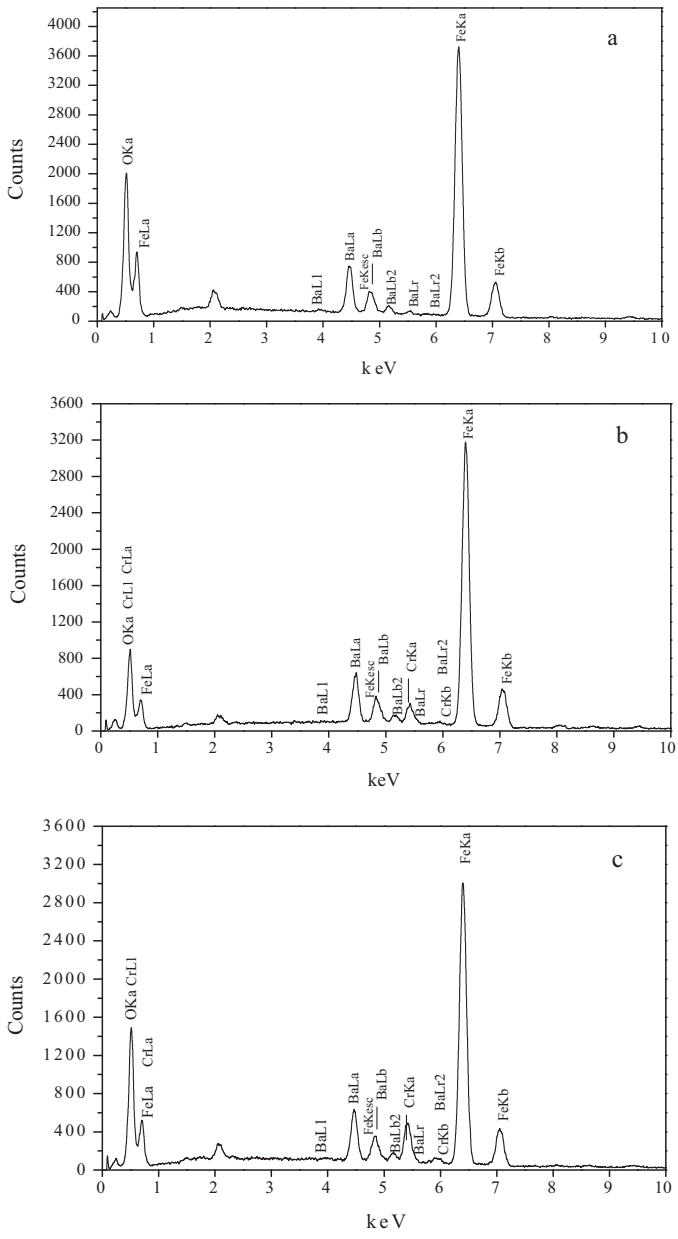

Fig. 3. Typical EDAX pattern of $BaFe_{12-x}Cr_xO_{19}$ for (a) x = 0.00, (b) x = 0.50, and (c) x = 1.00 samples.

formed as a resultant of agglomeration of individual nanoparticles. These SEM images were used to obtain the grain size. The average grain size obtained from SEM images is in the 40–60 nm range and is listed in Table 2.

3.4. Magnetic analysis

The magnetic behaviour of $BaFe_{12-x}Cr_xO_{19}$ (x = 0.00, 0.25, 0.50, 0.75, and 1.00) was recorded at room temperature by using vibrating sample magnetometer (VSM) technique at maximum field 9 kOe. The sample shows high coercivity and non saturation up to a field of 9 kOe. Non saturation behaviour of the samples may indicate the presence of some fraction of super paramagnetic particles in the sample or an additional phase such as α-Fe_2O_3. The presence of α-Fe_2O_3 which is canted antiferromagnet, may also contribute to the reduction in magnetization value [33]. The saturation magnetization (M_s), remanence magnetization (M_r), coercivity (H_c) of $BaFe_{12-x}Cr_xO_{19}$ samples decreases with increase in chromium con-

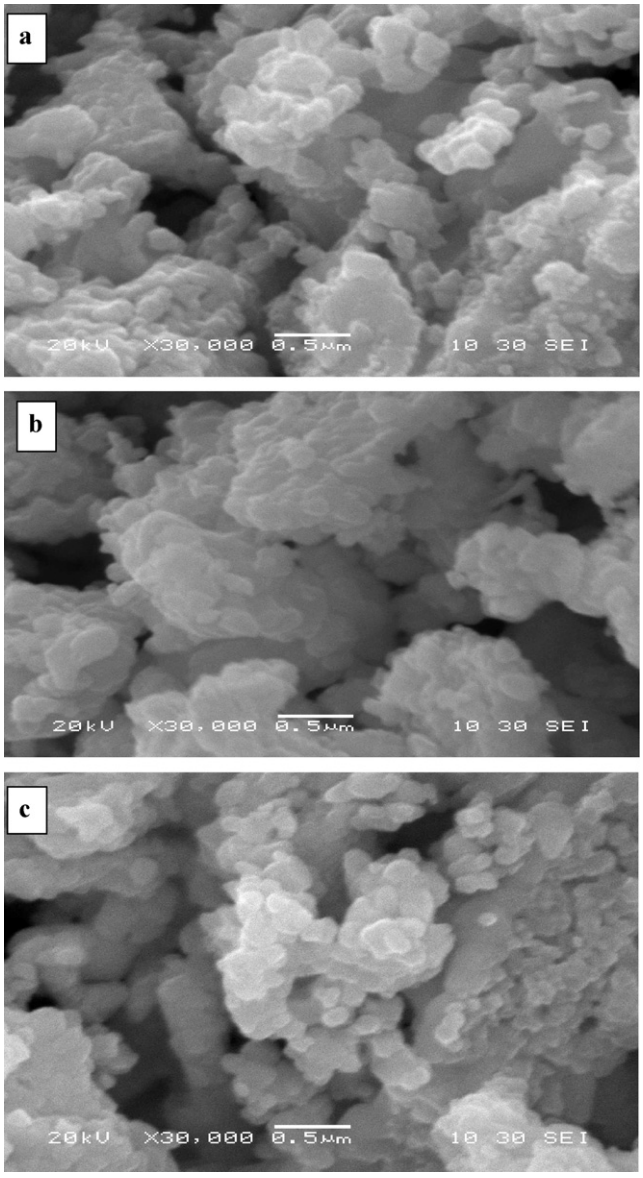

Fig. 4. Typical scanning electron microscope images of $BaFe_{12-x}Cr_xO_{19}$ at (a) $x = 0.00$, (b) $x = 0.50$ and (c) $x = 1.00$ samples.

tent. The decrease in magnetization is related to the magnetic moment of the constituent ions. In the present case Fe^{3+} ions having magnetic moment of 5 μ_B was replaced by Cr^{3+} ions which having 3 μ_B magnetic moment. Owing to the magnetic moment of Cr^{3+} (3 μ_B) ion is not able to cancel out with spin down moments of Fe^{3+} ions (5 μ_B). More specifically substitution causes weakening of super exchange interaction of type $Fe_A{}^{3+}$–O–$Fe_B{}^{3+}$, leading to collapse of magnetic collinearity of the lattice. The decrease in saturation magnetization and remanence magnetization with substitution of Cr^{3+} is closely agrees with the observations made for Al^{3+} and Mn^{3+} substituted barium hexaferrite prepared by glass ceramic technique and solution combustion technique [31,34,35].

The magneton number n_B (μ_B) is obtained by using the relation:

$$n_B = \frac{\text{Molecular weight} \times M_s}{5585} \quad (6)$$

where M_s is the saturation magnetization of the sample.

The values of magneton number n_B (μ_B) goes on decreasing with increase in Cr^{3+} substitution due to the replacement of less magnetic moment of Cr^{3+} (3 μ_B) as compared to Fe^{3+} (5 μ_B). The

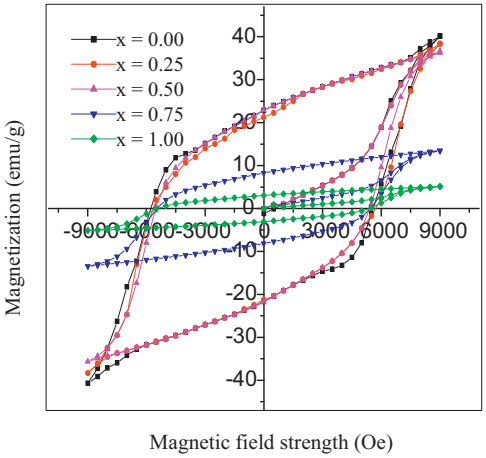

Fig. 5. Hysteresis plots of $BaFe_{12-x}Cr_xO_{19}$ samples.

Table 3
Saturation magnetization (M_s), remenant magnetization (M_r), coercivity (H_c) and magneton number (n_B) of $BaFe_{12-x}Cr_xO_{19}$ samples.

Comp. 'x'	M_s (emu/g)	M_r (emu/g)	H_c (Oe)	M_r/M_s	n_B (μ_B)
0.00	40.443	22.287	5689.28	0.5511	8.0486
0.25	38.390	21.250	5687.23	0.5535	7.6334
0.50	36.640	22.865	5464.80	0.6240	7.2791
0.75	13.491	8.264	5462.13	0.6125	2.6778
1.00	5.119	3.053	5396.41	0.5964	1.0152

hysteresis loops for Cr^{3+} substituted barium hexaferrite samples are depicted in Fig. 5. The values of saturation magnetization decreases from 40.433 emu/g to 5.113 emu/g and the values of coercivity decreases from 5689.28 Oe to 5396.41 Oe. The values of these magnetic parameters are listed in Table 3. From our results it is clear that the magnetic properties were influenced by Cr^{3+} substitution in the barium hexaferrite matrix.

4. Conclusions

Nanocrystalline chromium substituted barium hexaferrite samples have been successfully synthesized by sol–gel autocombustion technique. The X-ray diffraction pattern reveals the formation of M-phase hexagonal structure at $x = 0.00$, and for 0.25–1.00 (in the step of 0.25) shows α-Fe_2O_3 as a secondary phase. Energy dispersive analysis of X-rays confirms that the synthesized samples have attained the nominal theoretical stoichiometry. The lattice parameters a and c, X-ray density (d_x), particle size (t) decreases whereas porosity increases with increase in Cr^{3+} substitution x. SEM image shows the well agglomerated grains. The values of saturation magnetization, remanent magnetization and magneton number goes on decreasing with the increase in Cr^{3+} content x.

Acknowledgements

One of the authors (VND) is thankful to Dr. Babasaheb Ambedkar Marathwada University, Aurangabad (M.S.), India, for giving Golden Jubilee meritorious scholarship. Authors are also thankful to TIFR, Mumbai for providing XRD facility, Pune University, Pune (M.S.), India for providing SEM, EDAX and VSM facility.

References

[1] H. Pfeiffer, R.W. Chantrel, P. Gornert, W. Schuppel, E. Sinn, M. Rosler, J. Magn. Magn. Mater. 125 (1993) 373.
[2] J. Smit, H.P.J. Wijn, Ferrites, Philips Technical Library, Eindhoven, 1961.

[3] W. Buchner, R. Schliebs, G. Winter, K.H. Buchel, Industrial Inorganic Chemistry, V.C.H. Weinheim, 1989.
[4] R.B. Jotania, R.B. Khomane, A.S. Deshpande, C.C. Chauhan, B.D. Kulkarni, J. Sci. Res. 1 (2009) 1.
[5] A. Goldman, Modern Ferrite Technology, Springer, Berlin, 2006.
[6] B.B. Hovis, K.T. Faber, Scripta Mater. 44 (2001) 2525.
[7] A. Mali, A. Ataie, Scripta Mater. 53 (2005) 1065.
[8] P. Shephred, K.K. Malick, R.J. Green, J. Magn. Magn. Mater. 312 (2007) 418.
[9] J. Wang, Q. Chen, S. Che, J. Magn. Magn. Mater. 280 (2004) 281.
[10] G.P. Rodrigue, IEEE Trans. Microw. Theory Tech. 11 (1969) 351.
[11] Y. Chen, M.H. Kryder, IEEE Trans. Magn. 34 (1998) 729.
[12] A. Morisako, X. Liu, M. Matsumoto, J. Appl. Phys. 81 (1997) 4374.
[13] T. Ogasawara, M.A.S. Olieira, J. Magn. Magn. Mater. 217 (2000) 147.
[14] J. Matutes-Aquino, S. Diaz-castanon, Scripta Mater. 42 (2000) 295.
[15] L. Rezlescu, E. Rezlescu, P.D. Popar, N. Rezlescu, J. Magn. Magn. Mater. 193 (1993) 288.
[16] X. Liu, J. Wang, L.M. Gan, S.C. Ng, J. Magn. Magn. Mater. 195 (1999) 452.
[17] R.C. Pullar, A.K. Bhattacharya, J. Mater. Lett. 57 (2002) 537.
[18] J. Liu, W. Zhang, C. Guo, Y. Zeng, J. Alloys Compd. 479 (2009) 863.
[19] X. Liu, J. Wang, L.M. Gan, S.C. Ng, J. Ding, J. Magn. Magn. Mater. 184 (1998) 344.
[20] V.K. Sankarnarayanan, D.C. Khan, J. Magn. Magn. Mater. 153 (1996) 337.
[21] M.V. Cabans, J.M. Gonzalez-Calbet, M. Labeau, P. Mollard, M. Pernet, M. Vallet-Regis, J. Solid State Chem. 101 (1992) 265.
[22] H.F. Yu, H.-Y. Lin, J. Magn. Magn. Mater. 283 (190) (2004) 2–3.
[23] H.M. Lee, S.-Y. Bae, J.-H. Yu, Y.-J. Kim, J. Am. Ceram. Soc. 91 (9) (2008) 2856.
[24] J. Huang, H. Zhang, W. Li, J. Mater. Res. Bull. 38 (2003) 149.
[25] S.E. Jacobo, C. Domingo Pacual, M.A. Bleja, J. Mater. Sci. 32 (1997) 1025.
[26] A. Guruskova, J. Lipka, M. Papanova, J. Subrt, J. Hyperfine Interact. 164 (2005) 27.
[27] Z. Min-jiang, M.A. Hong-liang, H.E. Zheng-ming, J. Shanghai Univ. (English edition) 11 (2007) 263.
[28] H.F. Yu, K.C. Huang, J. Magn. Magn. Mater. 260 (2003) 455.
[29] H.Z. Wang, Q. He, G.H. Wen, F. Wang, Z.H. Ding, B. Yao, J. Alloys Compd. 504 (2010) 70.
[30] M.J. Iqbal, M.N. Ashiq, Chem. Eng. J. 136 (2008) 383.
[31] H. Fu, H.R. Zhai, Y.C. Zhang, B.X. Gu, J.Y. Li, J. Magn. Magn. Mater. 54–57 (1986) 905.
[32] B.D. Cullity, Elements of X-ray Diffraction, Addison-Wessley Publishing Company Ltd, 1959.
[33] D. Bahadur, S. Rajkumar, A. Kumar, J. Chem. Sci. 118 (1) (2006) 15.
[34] V.N. Dhage, M.L. Mane, A.P. Keche, C.T. Birajdar, K.M. Jadhav, Physica B: Condens. Mater. 406 (2011) 789–793.
[35] T. Suzuki, K. Kani, K. Warri, S. Kawakani, Y. Torii, J. Mater. Sci. Lett. 11 (1992) 883.